RSC Advances

ROYAL SOCIETY OF CHEMISTRY

PAPER

View Article Online
View Journal | View Issue

Cite this: *RSC Adv.*, 2025, **15**, 4332

Preparation of high-strength ceramsite from coal gangue, fly ash, and steel slag

Xi Chen,[*abc] Chenxi Zhang,[*c] Yuping Tong,[c] Xiao Wang,[c] Xiao Chen,[c] Yuandong Yang,[d] Jiayin Liu,[c] Qi Chen[c] and Ningning Li[c]

Received 18th November 2024
Accepted 14th January 2025

DOI: 10.1039/d4ra08140d

rsc.li/rsc-advances

Coal gangue (CG) and fly ash (FA) are generated in large quantities worldwide. In this study, high-strength and lightweight aggregate ceramsites were prepared from CG, FA, and steel slag (SS) without any additional chemical additives through high-temperature sintering. The study aimed at determine the sintering mechanism and optimal production process by evaluating the performance of ceramsites produced under various conditions. The results indicated that the ratio of CG, FA, and SS significantly influenced the ceramsites' properties. When the ratio of CG, FA, and SS was 3 : 1 : 1 and the sintering temperature was 1200 °C, the ceramsites demonstrated optimal performance. These ceramsites had a bulk density of 947 kg m^{-3}, an apparent density of 1859 kg m^{-3}, a high compressive strength of 21.17 MPa, and a 1 hour water absorption of 1.35%. The high-strength and lightweight aggregate ceramsites produced from CG, FA, and SS hold promise as construction materials, particularly due to the benefits of waste recycling. This study highlights the potential of utilizing these ceramsites as sustainable alternatives in various construction applications.

1 Introduction

With rapid industrial and economic development, the exploitation and utilization of resources have increased significantly, leading to the production of vast amounts of solid waste. This not only occupies valuable land resources but also poses potential risks to both human health and the environment, particularly due to the presence of hazardous waste.[1,2] Therefore, recycling and reusing solid waste as raw materials for the production of valuable products represents the most sustainable and environmentally friendly solution for managing the substantial waste generated each year.

Coal gangue, fly ash and steel slag are among typical solid waste. Coal gangue is waste residue discharged along with the coal mining process, accounting for about 15–20% of the output of raw coal.[3] Coal gangue contains some heavy metal elements; a large number of piles will cause pollution to the land.[4–6] Therefore, large amounts of coal gangue need to be handled properly. The composition of coal gangue mainly includes Si, Al, Fe, Ca, and Mg oxides, and several rare metals.[7,8] Currently, coal gangue has been used in various applications such as recovery of valuable elements, land reclamation and production of building materials. Qin *et al.*[9] used a low-temperature combined roasting-deionized water leaching method to extract valuable elements from coal gangue and prepare adsorbent materials. Wu *et al.*[10] prepared an eco-friendly low-carbon coal gangue pervious concrete using coal gangue. Li *et al.*[11] successfully prepared an activated catalyst conducive to the remediation of organic pollution in groundwater and soil using coal gangue and other activators. Although the gangue is traceable in many fields, at present China's utilization rate of the gangue is only about 50%; a large amount of gangue has not been reutilized.[4]

Fly ash is the main solid waste discharged from coal-fired power plants, and steel slag is mainly derived from oxides formed by molten iron and waste slag as one of the by-products of steelmaking.[12,13] Fly ash deposited for a long period of time contains traces of toxic heavy metal elements (Pb, Cr, Cu, Hg, *etc.*), so there is an urgent need to utilize them. Rafieizonooz *et al.*[14] conducted a feasibility study of fly ash as a cement substitute in concrete. Tabit *et al.*[15] studied the mechanism and optimization of ceramic formation using fly ash and steel slag as raw materials, and obtained ceramics with a compressive strength of 80 MPa. Guo *et al.*[16] prepared a ultra-high toughness fly ash/steel slag based geopolymer. Motz *et al.*[17] used fly ash, red mud and bentonite to obtain high strength ceramic granules with a barrel compressive strength of 30 MPa by optimizing the ratio and sintering conditions *etc.*

Ceramsite is a man-made aggregate consisting of an aluminum silicate phase, a feldspar phase, and a liquid phase. Ceramsites are used in the construction industry and other fields because of their light weight, high strength and earthquake resistance.[18–21] Cheng *et al.*[22] used fly ash as a raw

---

[a] *School of Food Science and Technology, Henan University of Technology, Henan, 450001, China. E-mail: chenxincwu@163.com*

[b] *Zhengzhou Zhongyuan Silande High Technology Co., Ltd, Henan, 450000, China*

[c] *School of Materials Science, North China University of Water Resources and Electric Power, Henan, 450045, China*

[d] *Henan GOODS and MATERIALS Group Corporation, Henan, 450007, China*

material to prepare ceramic granules with a microporous structure, which showed excellent performance in treating phosphorus polluted wastewater. Yu *et al.*[23] prepared lightweight and high strength ceramic granules by using steel slag, fly ash, and clay as raw materials. Sun *et al.*[24] prepared lightweight ceramic granules by optimizing the experimental conditions by using red mud as the main material. Most of the raw materials for pottery formation contain large amounts of SiO_2, Al_2O_3 and other aluminosilicates as well as some fluxes (CaO, Fe_2O_3, NaO, K_2O, *etc.*);[25] the raw material composition of gangue, fly ash and steel slag make it possible to use them as raw materials for the preparation of ceramsite. Coal gangue, fly ash and steel slag instead of non-renewable resources for the preparation of lightweight aggregates not only solves the problem of solid waste occupying resources and polluting the environment, but also comprehensively utilize a variety of solid waste, turning waste into treasure to improve the added value of solid waste.

Research on lightweight and high-strength ceramsites[26–30] is listed in Table 1. Ceramsites prepared from solid waste were widely used in functional and sustainable modern materials such as lightweight high-strength concrete, for water treatment, and so on.[31–35] The use of solid waste especially effectively reduces the carbon footprint of the mixture, which is beneficial to the development of cleaner production technologies.[36] By utilizing industrial by-products such as coal gangue, fly ash, and steel slag, this approach promotes waste recycling and reduces the need for virgin raw materials. This helps minimize resource extraction, energy consumption, and associated greenhouse gas emissions. Additionally, the production of ceramsite as a lightweight aggregate can result in lower emissions in the manufacturing of concrete and other construction materials, thereby reducing the carbon footprint of the construction industry, which is one of the largest contributors to global carbon emissions. Thus, this innovative material aligns with the United Nations' Sustainable Development Goals (SDGs).

In this study, in order to recycle and reuse the three materials coal gangue, fly ash and steel slag, a novel coal gangue-based high-strength ceramsite was firstly prepared with coal gangue as the main raw material, fly ash and steel slag as auxiliary materials without any admixture. The effects of preheating temperature, roasting temperature, sintering residence time and raw material ratio are investigated, and the compressive strength, water absorption, bulk density and apparent density of ceramsite were tested through the light aggregate test method in GTB/17431.2. The results enrich the Riley phase diagram and provide a simple and convenient method for the preparation of light and high strength ceramsite. The sintering mechanism, heavy metal leaching, the crystalline phase and micromorphology of the ceramsite are characterized and analyzed by DSC, FTIR, ICP-OES, XRD and SEM.

2 Experimental section

2.1 Material characteristics

The raw materials used in this study were coal gangue, fly ash and steel slag. Coal gangue (CG) (Fig. 1(a)) was obtained from Shenhuo Liangbei Mining Field, Yuzhou City, Henan Province, China, and FA (Fig. 1(b)) was obtained from Dengfeng Power Plant, Zhengzhou City, China. SS (Fig. 1(c)) was sourced from Wugang Industrial Company, Pingdingshan City, Henan Province, China.

The chemical compositions of these materials were determined by X-ray fluorescence spectrometer (XRF) (ARL FORM'X).Table 2 lists the main chemical compositions of these materials. Fe_2O_3 content was the highest in steel slag, followed by CaO. The content of SiO_2 in gangue was the highest, followed by Al_2O_3.The mineral compositions of the raw materials (as shown in Fig. 2) were determined by X-ray diffractometer (XRD) (Bruke D8 Advance), scanning from 10° to 80° at a rate of

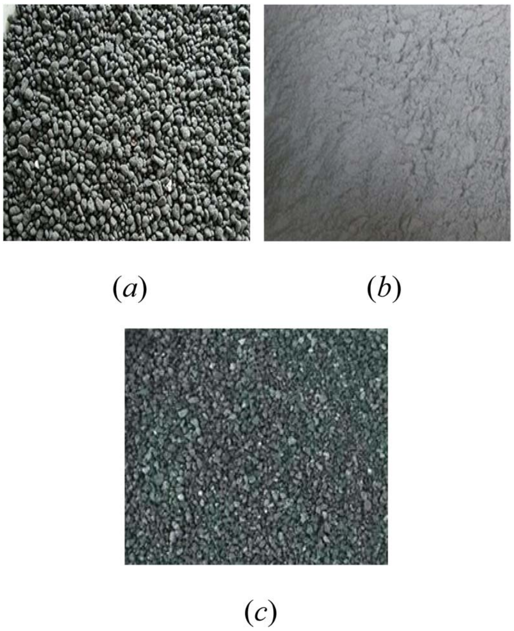

Fig. 1 Appearance of raw materials: CG (a), FA (b) and SS (c).

Table 1 The research on lightweight and high-strength ceramsite

Raw material	Sintering condition	Density/strength	Ref.
Red mud, coal fly ash	1200 °C – 5 min	$\leq$0.93 g cm^{-3}/1.08 kN	26
River bottom silt, waste oil sludge, paint bucket slag, 1% SiC	1180 °C – 10 min	490 kg m^{-3}/2.15 MPa	27
Coal-based solid waste, industrial sludge	1175 °C – 15 min	998 kg m^{-3}/27.26 MPa	28
MSWI fly ash, kaolin	1150 °C – 15 min	—/24.8 MPa	29
Lightweight MSWI fly ash, granite sawing mud	1150 °C – 20 min	986 kg m^{-3}/16.97 MPa	30

Table 2 Chemical compositions of gangue, fly ash and steel slag

Components (wt%)	SiO_2	Al_2O_3	Fe_2O_3	CaO	NaO	K_2O	MgO	TiO_2	Other
Coal gangue	58.48	31.73	1.96	1.89	1.19	2.34	0.55	1.14	0.72
Fly ash	63.05	13.67	6.74	3.91	3.10	4.15	2.15	1.01	2.22
Steel slag	15.68	4.67	32.34	34.23	0.12	0.05	3.66	0.98	8.27

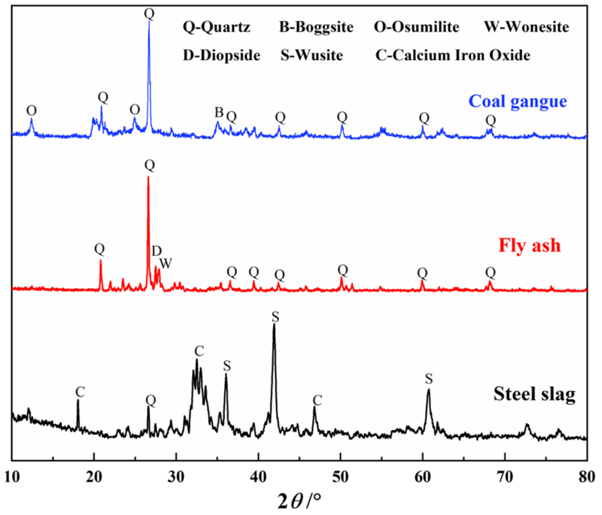

Fig. 2 XRD patterns of raw materials.

5° min^{-1}. The main mineral components of coal gangue were quartz (SiO_2), boggsite ($NaCa_2Al_5Si_{19}O_{48}\cdot17(H_2O)$) and osumilite ($2Al_2[Al_3Si_9O_{30}]\cdot H_2O$). The SS is black in color because of the existence of calcium iron oxide. The main mineral components of fly ash were quartz (SiO_2), wonesite ($(Na,K)_{0.5}(Mg,Fe,Al)_3(Si,Al)_4O_{10}(OH, F)_2$) and diopside ($CaMg(SiO_3)_2$).

2.2 Preparation of aggregate ceramsites

Based on Riley phase as showed in Fig. 3, the three types of powder were proportioned according to Table 3 and mixed uniformly. Batch 1 samples were in comparison of different material proportion while batch 2 samples, all made with CG 60%–FA 20%–SS20%, were for comparing different calcination temperatures.

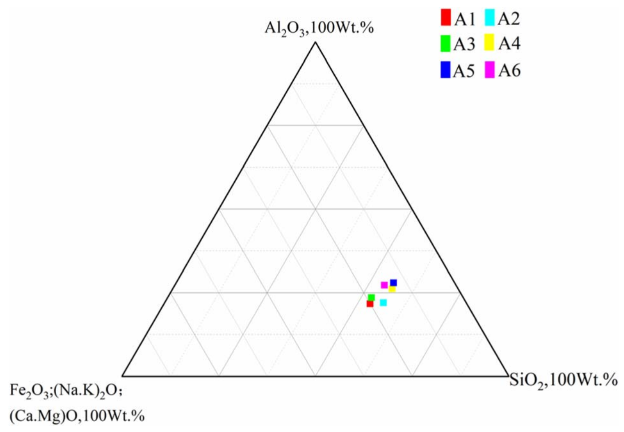

Fig. 3 Ternary phase diagram of ceramsite with different proportions.

Fig. 4 outlines the preparation process of ceramsites. Raw materials (*i.e.* CG, FA and SS) were crushed and grind through jaw crusher, and then passed through a 0.45 mm sieve. The three raw materials are uniformly mixed at 2800 rpm for 1 h by the mixer according to Table 3 with 20 wt% water. The stirred mixtures were put into a desktop granulator for mechanical extrusion molding, and then 7–8 mm diameter balls were obtained. Further shaping the particle shape to achieve a smooth edge, the balls were placed into a disc granulator with a speed of 40 rpm and a disc inclination angle of 60°. And then they were placed in an oven with temperature of 105 °C for drying to constant weight. The fresh pellets prepared by this method could meet the requirements of the graduation in standard (GB/T 17461.1-2010). The subsequent sintering process in a muffle furnace was divided into two stages, namely pre-calcination and calcination. The pellets were heated up at 10 °C min^{-1}, maintaining the temperature at 450 °C for 15 min and 1200 °C for 10 min. After completion of the sintering process, the pellets were taken out from the muffle furnace immediately for cooling at room temperature.

2.3 Test methods

The bulk density, apparent density, porosity and 1 hour water absorption of lightweight aggregates were tested in accordance with Chinese standards (GB/T 17431.1-2010 and GB/T 17431.2-2010).

2.3.1 Strength. In order to measure the strength of ceramsites accurately, a microcomputer controlled universal material testing machine (HDW-50A) was used. 30 samples were selected from each group. The calculation of strength (MPa) S was according to the following formula:

$$S = \frac{2.8 \times P_c}{\pi X^2}$$

where P_c is the crushing load (N), and X is the distance between the upper and lower loading plates (mm).

2.3.2 1 Hour water absorption. The change in water absorption of ceramsites is an important factor affecting their porosity and strength. It is reported that the water absorption was inversely proportional to strength and directly proportional to the porosity in previous research. The calculation of 1 hour water absorption rate (%) w_a was according to the following formula:

$$w_a = \frac{m_0 - m_1}{m_1} \times 100\%$$

Table 3 Summary of material proportions and sintering temperatures

Batch 1			Batch 2	
Sintering at 1200 °C			CG 60%–FA 20%–SS 20%	
Sample label	Material proportion	Chemical proportion	Sample label	Sintering temperature/°C
A1	CG 50%–FA 30%–SS 20%	SiO_2 51.3%–Al_2O_3 20.9%–RO/R_2O 24.0%	B1	1050 °C
A2	CG 50%–FA 40%–SS 10%	SiO_2 56.0%–Al_2O_3 21.8%–RO/R_2O 21.2%	B2	1100 °C
A3	CG 60%–FA 20%–SS 20%	SiO_2 50.8%–Al_2O_3 25.4%–RO/R_2O 22.8%	B3	1150 °C
A4	CG 70%–FA 20%–SS 10%	SiO_2 55.1%–Al_2O_3 27.2%–RO/R_2O 16.6%	B4	1200 °C
A5	CG 80%–FA 10%–SS 10%	SiO_2 54.6%–Al_2O_3 27.2%–RO/R_2O 15.4%	B5	1250 °C
A6	CG 80%–FA 20%	SiO_2 53.1%–Al_2O_3 26.8%–RO/R_2O 18.1%		

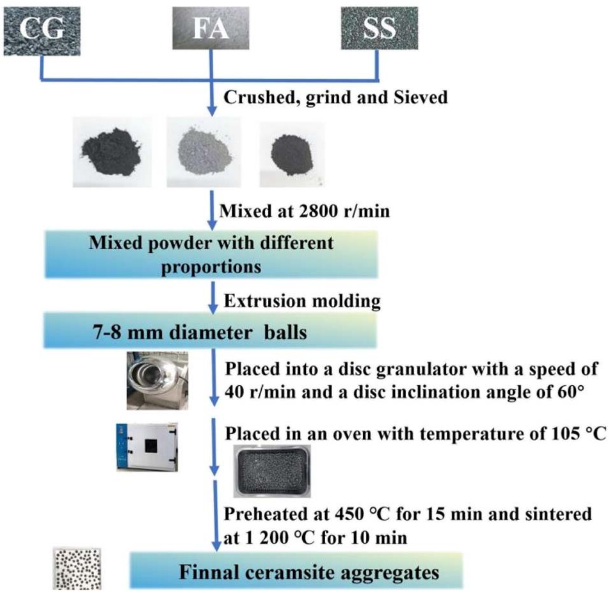

Fig. 4 Production process of ceramsite aggregates.

where m_0 is the mass of the ceramsites soaked for 1 h (g), m_1 is the mass of the ceramsites after drying (g).

2.3.3 Apparent density and bulk density. Firstly dried ceramsites m (g) were soaked in water for 1 hour, then the surface moisture on the ceramsites was wiped off after filtration. Finally, the ceramsites were placed into a 1000 ml cylinder filled with 500 ml of water and the total volume V_t (mL) is recorded. The apparent density ρ_{ap} (kg m^{-3}) was calculated using the following equation:

$$\rho_{ap} = \frac{m \times 1000}{V_t - 500}$$

The ceramsites m (g) were evenly poured into a 1 L capacity cylinder up to 50 mm above the mouth. The excess ceramsites at the top of the cylinder were scraped away with a ruler, and any surface depressions were filled with fine particles. The bulk density ρ_b (kg m^{-3}) was calculated using the following formula:

$$\rho_b = \frac{(m_t - m_v) \times 1000}{V}$$

where m_t is the total mass of the sample and the cylinder (kg), m_v is the mass of the cylinder (kg), and V is the volume (L) of the cylinder.

3 Results and discussion

3.1 Characteristics of ceramsite

3.1.1 Physicochemical performance of ceramsite. The ceramsites made in the experiment are shown in Fig. 5. It can be observed that the ceramsites made from different proportions have visual differences. Too high Si/Al ratio will increase the sintering temperature, and less liquid phase production is not conducive to mass transfer and migration between particles, resulting in a loose surface; However, a low Si/Al ratio will result in a decrease in strength. The raw materials contain different proportions of alkali metal oxides such as Fe, K, Na, Ca, Mg, *etc.*, which can form low melting point eutectic compounds with Si and Al, thereby producing a liquid phase and promoting mass transfer and migration between particles.

The results of density, porosity, compressive strength, and water absorption of the prepared ceramsite were shown in Fig. 6 and 7. With the increasing gangue content, the compressive strength gradually decreased, and the strength of ceramics was greater when the gangue content was 50% and 60%, which were 25.58 MPa, 15.81 MPa and 19.15 MPa, respectively. Although the increase of Al_2O_3 content has an effect on the strength of ceramsite, excessive Al_2O_3 and SiO_2 increase the eutectic temperature, resulting in incomplete sintering. On the other hand, the low supporting component is not conducive to the generation of liquid phase, and cannot better promote the sintering reaction. The higher strength of A3 than A2 is due to the increase in Fe and Ca content affecting the structure and

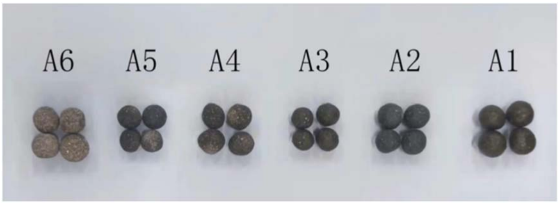

Fig. 5 Photos of sintered ceramsites made from CG, FA and SS with different proportions.

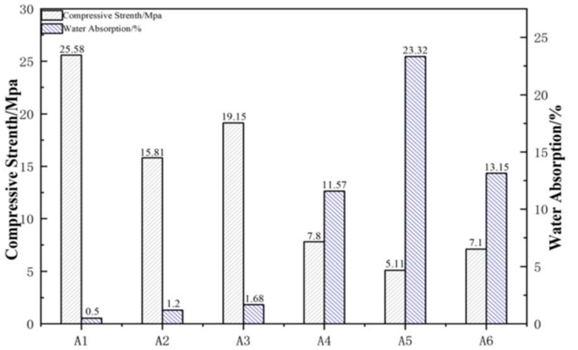

Fig. 6 Compressive strength and water absorption of ceramsites produced from different mixtures.

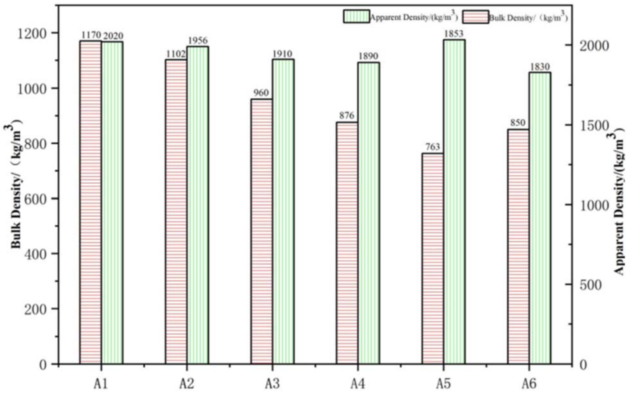

Fig. 7 Bulk density and apparent density of ceramsites produced from different mixtures.

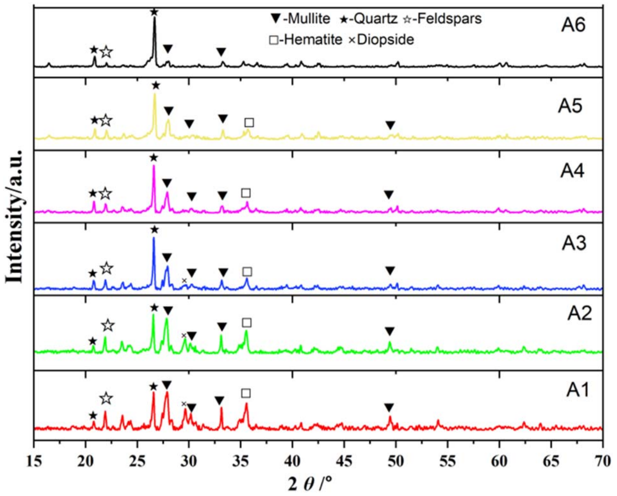

Fig. 8 XRD at different proportions.

composition of ceramsite. Water absorption first rises and then decreases, which is related to the enamel produced on the surface of the ceramic grain, as shown in Fig. 7. The lower water absorption ensures a more stable application performance of ceramic particles in concrete. With the increase of the solubility component, a dense enamel layer is formed on the surface of the ceramic grain, resulting in a decrease in water absorption and an increase in strength. The bulk density and apparent density of A1, A2 and A3 were 1170 kg m^{-3}, 1102 kg m^{-3}, 960 kg m^{-3} and 2020 kg m^{-3}, 1990 kg m^{-3} and 1910 kg m^{-3}, respectively. Considering the high compressive strength, low water absorption and relatively low density, the ceramsite with suitable properties could be obtained when the proportion of CG : FA : SS was 6 : 2 : 2.

3.1.2 Mineralogical characterization of ceramsites. The XRD patterns of the ceramsite in different proportion of raw materials were presented in Fig. 8. The crystal phases of A1, A2, and A3 samples include calcium feldspar ($CaAl_2Si_2O_8$), sodium feldspar ($NaAl_2Si_3O_8$), hematite (Fe_2O_3), diopside ($CaMgSi_2O_6$), and mullite ($Al_6Si_2O_{13}$). For A4–A6, the crystal phases are primarily quartz (SiO_2), mullite, feldspar and hematite. As the coal gangue content increases,the diffraction peak of the feldspar phase weakens. This suggests that with the increasing SiO_2 content, the required sintering temperature rises, leading to incomplete sintering. Additionally, at 33.5°, the diffraction peak of the mullite phase ($Al_6Si_2O_{13}$) diminishes, further indicating that the higher intensities in A1–A3 are attributed to the greater formation of feldspar and mullite phases, which enhances the strength of the ceramic particles. Moreover, the diffraction peak of pyrite disappears, replaced by that of hematite. This is due to the oxidation of iron ore to hematite (Fe_2O_3) at high temperatures. As the steel slag content increases, the interaction of CaO, FeO, and SiO_2 forms a low-temperature eutectic feldspar, which remains in the liquid phase at around 1000 °C. With the increase of Fe and Ca content, the liquid phase content and viscosity in the multi-component system gradually decreased and the melting temperature range became wider.[37] This lowers the sintering temperature and promotes the formation of new phases. The dark black color of A1–A5, which contains steel slag, is due to the presence of goethite (FeO) in the raw materials, which oxidizes to Fe_2O_3 at high temperatures. In contrast, A6, which does not contain steel slag or goethite, exhibits a light yellow color.

It can be seen in Fig. 9 that the A1, A2, and A3 samples contain uniformly distributed closed pores, with a significant amount of liquid phase surrounding the pores, resulting in a relatively dense structure. The presence of the liquid phase facilitates the sintering process, which also indicates that the

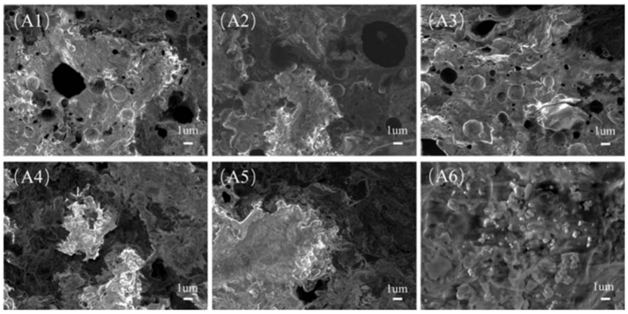

Fig. 9 SEM at different proportions.

incorporation of steel slag and fly ash promotes the gas generation. During sintering, the gas produced is encapsulated by the liquid phase, forming closed pores, which helps to reduce the weight of the ceramsite. In contrast, with the increasing content of coal gangue, the A4, A5, and A6 samples exhibit interconnected open pores and noticeable unreacted substances. Incomplete reactions, as well as weak particle migration and mass transfer, hinder the formation of new phases and lead to incomplete sintering, resulting in a decrease in the strength of the ceramsite.

3.2 Effect of calcination temperature on properties of ceramsites

The sintering temperature has a great influence on the performance of the ceramic grain, that is, insufficient sintering will cause the high strength of ceramsite, which excessive sintering will lead to the collapse of the ceramsite' structure, and the liquid phase will occur too much melting and bonding. The sintering temperature 1050 °C, 1100 °C, 1150 °C, 1200 °C and 1250 °C were settled to reveal the effect of sintering temperature on the properties of A3.

The intensity, water absorption, bulk density, apparent density, morphology,porosity and XRD of the samples are shown in Fig. 10–14, respectively. At sintering temperature 1050 °C to 1100 °C, the sample surface has obvious open pores and large particle gaps, and the ceramsite are light gray; the small amount of liquid phase was generated on the surface of the sample at 1150 °C, the pores of the surface opening were relatively reduced, and the sample was dark gray; a large amount of liquid phase is generated on the surface of the 1200 ° C and 1250 °C samples, and the open pores are filled with the liquid phase, and the sample is brown. The strength and bulk density increase with the increase of sintering temperature before 1200 °C, and the water absorption rate and apparent density decrease. This is due to the fact that as the sintering temperature increases, the ceramic grain produces a large amount of liquid phase to fill the open pores of the surface, and the enamel is produced to make the ceramic grain dense.

The strength, water absorption, bulk density and apparent density of ceramsite at 1200 °C were 19.15 MPa, 1.68%, 960 kg m^{-3} and 1910 kg m^{-3}, respectively. At this temperature, due to the formed surface tension, the gas inside the ceramic grain reaches a dynamic equilibrium to form a uniform pore structure, so the strength increases. As the sintering temperature increases to 1250 °C, the ceramsite melts bond, the bottom structure collapses, and the strength of the ceramsite drops sharply. This is due to the excessive sintering to produce a large number of liquid phases, and too many amorphous phases are formed under the action of K, Na, Fe and other soluble components, resulting in large structural deformation and therefore reduced strength. At lower sintering temperatures, the sintered pellets have not yet reached the sintering temperature, and the pellet bodies are relatively loose with many internal pores, resulting in a relatively low bulk density. At higher sintering temperatures,

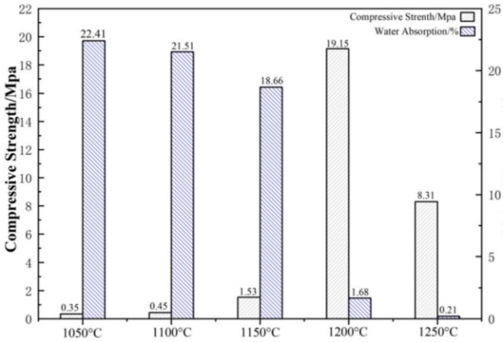

Fig. 10 Strength and water absorption of ceramsite at different temperatures.

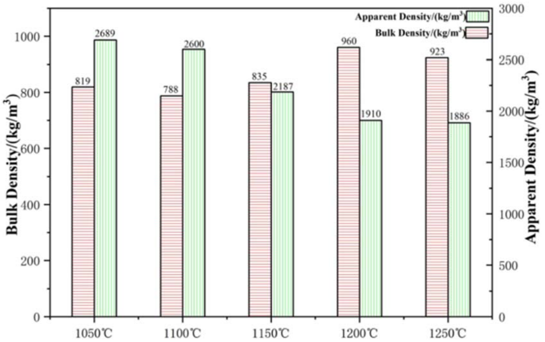

Fig. 11 Bulk density and apparent density of ceramsite at different sintering temperatures.

Fig. 12 Morphology of ceramsite at different sintering temperatures.

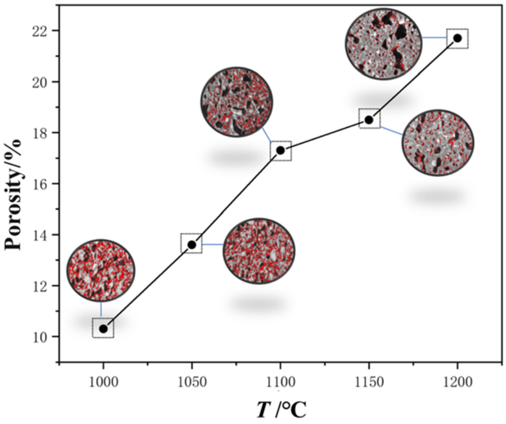

Fig. 13 Porosity of ceramsite at different sintering temperatures.

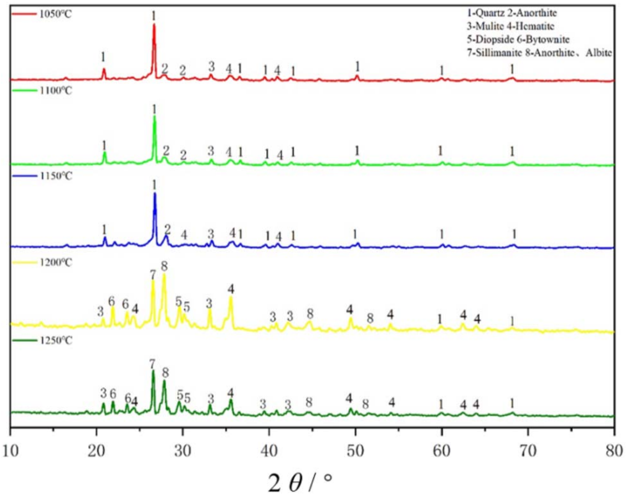

Fig. 14 XRD of samples at different temperatures.

the sample reaches the sintering temperature range, and the fluxing effect of the steel slag becomes more significant. As the temperature increases, the liquid phase in the ternary eutectic system increases. As the density of the ceramic pellets increases, the liquid phase infiltrates the pores under the action of surface tension, causing a continuous reduction in the visible porosity and an increase in the closed porosity within the sample. This leads to a decrease in water absorption and a relative increase in bulk density. However, when the sintering temperature is further increased, excessively high temperatures will generate more liquid phase, resulting in an excessive formation of amorphous phase. During the cooling process of the ceramic pellets, most of the liquid phase solidifies into a glassy phase, which has lower strength and causes significant structural deformation, preventing the ceramic pellets from forming into spheres. In order to obtain ceramsite with excellent performance, a sintering temperature of 1200 °C was selected for subsequent experiments.

As the sintering temperature increases, the porosity also increases, reaching a maximum of 21.46% at 1200 °C. This can be attributed to the higher sintering temperature, which promotes the formation of a greater amount of glass phase within the ceramic particles and enhances the liquid-phase mass transfer. As a result, smaller pores coalesce into larger ones due to the effect of liquid-phase mass transfer.

The XRD pattern of the sample is significantly influenced by the calcination temperature. After high-temperature calcination, numerous dispersed peaks appear in the XRD pattern of the ceramic particles, indicating that the internal structure of the ceramic particles primarily consists of an amorphous glass phase. At sintering temperatures of 1050 °C, 1100 °C, and 1150 °C, the crystal phases identified in the sample include SiO_2 (quartz), Fe_2O_3 (hematite), $3Al_2O_3\cdot 2SiO_2$ (mullite), and 4(Na,Ca)Al(Si, Al)$_3$O$_8$ (feldspar), with the same mineral phases observed at all these temperatures. When compared to the XRD pattern of the raw material, no phase changes are evident, suggesting that at these temperatures, the system is primarily in a surface mass transfer stage, with lower lattice activation energy and minimal chemical reactions. As the sintering temperature increases, the diffraction peaks of quartz gradually disappear or weaken, being replaced by the newly formed sillimanite. The intensity of the diffraction peaks corresponding to feldspar increases, and the crystal phases observed at this stage are feldspar (4(Na, Ca)Al(Si, Al)$_3$O$_8$), sillimanite (Al_2SiO_5), and hematite (Fe_2O_3). As the sintering temperature increases, the diffraction peak intensity of feldspar and mullite crystals increases, indicating that the increase in sintering temperature is beneficial to promote the formation of new phases. At sintering temperatures of 1050 °C, 1100 °C, and 1150 °C, some diffraction peaks of pyrite (FeO) disappear, while diffraction peaks of hematite (Fe_2O_3) emerge. This is due to the oxidation of FeO to Fe_2O_3 at high temperatures, which then reacts with CaO to form calcium iron garnet. Consequently, the ceramic particles maintain a light yellow color at these temperatures.

As the temperature increases, particularly at 1200 °C, the intensity of the diffraction peak for hematite strengthens, and the ceramic particles turn dark black. Additionally, the diffraction peak of quartz disappears. This change is attributed to the promotion of reactions between free quartz and alumina at the higher sintering temperature, leading to the formation of silicates. The diffraction peaks of feldspar and hematite also become more pronounced, due to the increased sensitivity of Ca^{2+} and Fe^{3+} ions at high temperatures. These ions exhibit strong nucleating abilities and serve as activation centers. The ionic radii of Ca^{2+} and Fe^{3+} are similar to that of Al^{3+}, allowing them to form solid solutions with aluminosilicates. However, during sintering, Fe^{3+} undergoes a reduction reaction, which alters its ionic radius and induces lattice distortion in the aluminosilicate structure. This reduction in ionic radius lowers the sintering temperature and accelerates the sintering process.

Calcium feldspar and sodium feldspar are freely miscible, meaning there is no pure phase of either calcium feldspar or sodium feldspar. At a sintering temperature of 1250 °C, the diffraction peak of feldspar decreases compared to the intensity observed at 1200 °C. This is because, at higher temperatures, a greater amount of liquid phase forms in the system, dissolving some of the feldspar and transforming its lattice from crystalline to amorphous. The reaction process is as follows:

$$3C + 2O_2 \rightarrow CO_2\uparrow + 2CO\uparrow$$

$$2CaCO_3 \rightarrow 2CaO + 2CO_2\uparrow$$

$$Al_2O_3 + SiO_2 \rightarrow Al_2SiO_5$$

$$CaO + Al_2O_3 + 2SiO_2 \rightarrow Ca(Al_2Si_2O_8)$$

$$Na_2 + Al_2O_3 + 6SiO_2 \rightarrow 2NaAlSi_3O_8$$

$$4NaAlSi_3O_8 + 4CaO + 10Al_2O_3 \rightarrow 4(Na, Ca)Al(Si, Al)_3O_8 + 17O_2\uparrow$$

$$nAl_2O_3 + nSiO_2 + K_2O + Na_2O + CaO + Fe_2O_3 \rightarrow \text{Feldspar}$$

3.3 Effect of calcination time on properties of ceramsites

Sintering time is also the main factor affecting the performance of ceramics, too short or too much sintering time will change the performance of ceramics. Sintering time of 10 min, 15 min, 20 min, 25 min, and 30 min are selected respectively. Morphology of ceramsite synthesized at different sintering time was shown in Fig. 15. With the extension of the sintering time, the color of the enamel layer on the surface of the ceramic grain gradually deepens, but slight adhesion occurs at 30 min.

The strength, water absorption, bulk density and apparent density of ceramics at different sintering times were shown in Fig. 16 and 17. With the increase of sintering time, intensity increased firstly and then decreased, the maximum was 21.17 MPa at 15 min, and the bulk density and apparent density gradually decreased. It was attributed to the increase of sintering time, more gas was generated inside the ceramic grain and was wrapped in the liquid phase in the ceramic grain, and the pores become more and form connected large pores, resulting in a decrease in density and strength; the strength of the ceramics grain is partly due to the provision of the newly generated mineral phase, and prolonged sintering can hinder the nucleation and growth of the internal feldspar and mullite phase crystals, reducing the strength. The water absorption rate is between 0.93% and 1.68%, and the change is not obvious. A large amount of liquid phase has been formed at the sub-sintering temperature, and the surface is densified after cooling, so it has little effect on water absorption. Considering lower density and high strength, the sintering time is selected to be 15 min.

Fig. 15 Morphology of ceramsite at different sintering time.

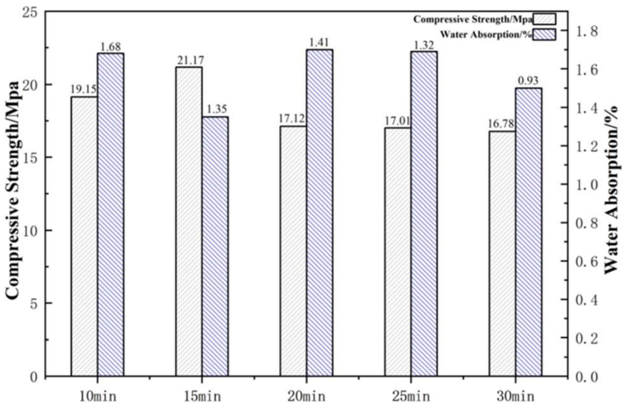

Fig. 16 Strength and water absorption of ceramsite at different sintering time.

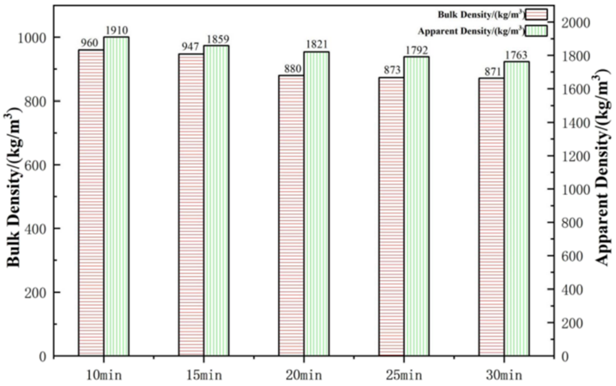

Fig. 17 Bulk density and apparent density of ceramsite at different sintering time.

3.4 Morphological characterization of ceramsite

SEM images of fracture surfaces and component analysis of ceramsite with CG/FA/SS 6 : 2 : 2 were shown in Fig. 18 and Table 4. Individual pores and new crystals could be observed clearly. The formation of the pores was due to the release of the internal gas and pore-making agent. Some of the fine micropores are filled with the liquid phase, which reduces the bulk density of the ceramsite. The rod-like feldspar crystals are interlaced with the flakyoxene crystals to form a grid, which improves the compressive strength of the ceramsite; at the same time, it prevents heavy metals from leaching from the pottery.

According to Table 4, the EDS analysis of the ceramsite indicated that the SiO_2 content is approximately 31.21%, Al_2O_3 is 26.73%, and CaO is 15.11%. The Si/Al ratio is determined to be about 1 : 1, and the (Ca, Na, K, Mg)/(Si, Al) ratio is also approximately 1 : 1, which falls within the elemental composition range typical of feldspar crystals. The presence of Fe^{3+} in the raw material is noteworthy, as its ionic radius is similar to that of Al^{3+}, allowing it to undergo an infinite solid solution with

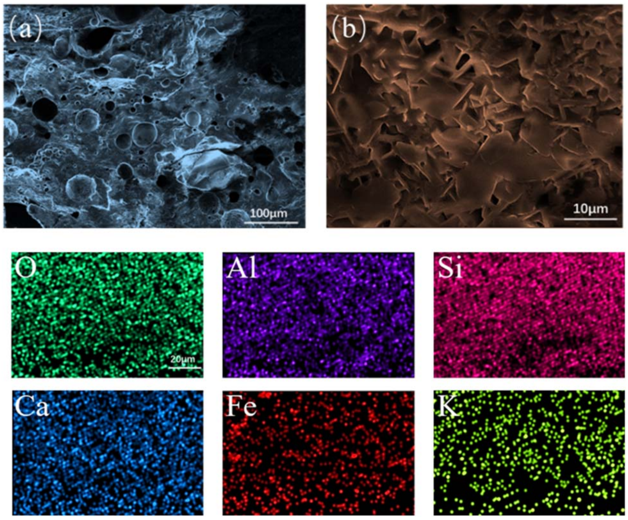

Fig. 18 Cross section of ceramsite at 1000 magnification (a) and cross section of ceramsite at 5000 magnification (b).

Table 4 Component analysis of ceramsite with CG/FA/SS 6 : 2 : 2 in SEM images

mol%	SiO_2	Al_2O_3	CaO	Fe_2O_3	Na_2O	MgO	K_2O
	31.21	26.73	15.11	8.12	5.57	1.12	1.36

Table 5 The result of the TCLP of ceramsites

Items	Pb	Zn	Ba	Cr	Ni
GB 3838-2022 (mg L^{-1})	0.01	1.0	0.7	0.05	0.02
Ceramsite (mg L^{-1})	0.0027	ND	ND	0.0003	0.001

aluminosilicates. At high temperatures, Fe^{3+} integrates into the oxygen tetrahedra of feldspar, resulting in a Fe_2O_3 content of 8.12% in the feldspar crystal.

3.5 Leaching concentrations of heavy metals in ceramsites

The compositions of the adsorbents were investigated using an ICP-MS apparatus. The heavy metal leaching toxicity analysis was conducted by GB 3838-2022 standard. The leaching concentrations of heavy metals in ceramsite did not exceed the limits for hazardous waste as showed in Table 5. Thus, the ceramsite could not be classified as hazardous waste. For the ceramsite, the leaching concentrations of heavy metals were much lower than the limits, it was because of the solidification effect of ceramsite on heavy metals. Indeed, the ceramsite got a stable characteristic after being sintered.

4 Conclusions

High-strength ceramsite was synthesized using gangue, fly ash, and steel slag through a two-stage sintering process. The influence of various factors, including the raw material weight ratio and sintering conditions (pre-heating temperature, sintering time, and sintering temperature), was systematically investigated. The effects of these parameters on the properties of the ceramsite were also determined. The mineral compositions, crystalline phases, microstructure, and hazardous substances solidification were determined by X-ray fluorescence spectrometry, X-ray diffraction analysis, Fourier transform infrared spectroscopy, scanning electron microscopy, and inductively coupled plasma optical emission spectroscopy. Under the optimal synthetic conditions (gangue : fly ash : steel slag = 60 : 20 : 20, preheating temperature of 450 °C, preheating time of 15 min, sintering temperature of 1200 °C, and sintering time of 15 min), the ceramsite demonstrated high compressive strength of 21.17 MPa, 1 h water absorption of 1.35%, and bulk density and apparent density were 947 and 1859 kg m^{-3}, respectively. Furthermore, the concentrations of toxic substances leaching from the ceramsite were considerably lower than the Chinese national standard (GB 3838-2002), which implies that gangue-based ceramsite cannot cause secondary environmental pollution. The prepared ceramsite exhibiting a high compressive strength, low water absorption, and effective solidification of deleterious elements can be used to prepare building concrete and lightweight partition boards. Importantly, the reuse of gangue for the production of ceramsite is an effective approach for the disposal of harmful gangue.

Data availability

The data are available from the corresponding author on reasonable request.

Conflicts of interest

There are no conflicts to declare.

Acknowledgements

Financial support is gratefully acknowledged from Natural Science Foundation of Henan 242300420561.

Notes and references

1 Y. Feng, W. Qi, Q. Zhao, Y. Huang, Q. Ren, W. Qi and F. Kong, Synthesis and characterization of cemented paste backfill: Reuse of multiple solid wastes, *J. Cleaner Prod.*, 2023, **383**, 135376.
2 X. Duan, Y. Huang, Y. Li, W. Zhang and Z. Huang, Evolution mechanism of pore structure in sintered coal gangue ceramsites, *Ceram. Int.*, 2023, **49**, 31385–31395.
3 Y. Chen, S. Zhou and W. Zhang, Effect of Coal Gangue with Different Kaolin Contents on Compressive Strength and Pore Size of Blended Cement Paste, *J. Wuhan Univ. Technol., Mater. Sci. Ed.*, 2008, 12–15.
4 J. Li and J. Wang, Comprehensive utilization and environmental risks of coal gangue: A review, *J. Cleaner Prod.*, 2019, **239**, 117946.
5 X. Y. Cong, S. Lu, Y. Yao and Z. Wang, Fabrication and characterization of self-ignition coal gangue autoclaved aerated concrete, *Mater. Des.*, 2016, **97**, 155–162.
6 H. Liu and Z. Liu, Recycling utilization patterns of coal mining waste in China, *Resour., Conserv. Recycl.*, 2010, **54**, 1331–1340.
7 L. Han, W. Ren, B. Wang, X. He, L. Ma, Q. Huo, J. Wang, W. Bao and L. Chang, Extraction of SiO_2 and Al_2O_3 from coal gangue activated by supercritical water, *Fuel*, 2019, **253**, 1184–1192.
8 J. Li, Y. Cao, A. Sha, R. Song, C. Li and Z. Wang, Prospective application of coal gangue as filler in fracture-healing behavior of asphalt mixture, *J. Cleaner Prod.*, 2022, **373**, 133738.
9 S. Qin, Q. Lu, Y. Li, J. Wang, Q. Zhao and K. Gao, Relationships between trace elements and organic matter in coals, *J. Geochem. Explor.*, 2018, **188**, 101–110.
10 C. Wu, C. Zhang, J. Li, X. Wang, W. Jiang, S. Yang and W. Wang, A sustainable low-carbon pervious concrete using modified coal gangue aggregates based on ITZ enhancement, *J. Cleaner Prod.*, 2022, **377**, 134310.

11 C. Li, S. Yin, Y. Yan, C. Liang, Q. Ma, R. Guo, Y. Zhang, J. Deng and Z. Sun, Efficient benzo(a)pyrene degradation by coal gangue-based catalytic material for peroxymonosulfate activation, *J. Environ. Manage.*, 2024, **351**, 119645.

12 D. Liang, J. Huang, Y. Zhang, Z. Zhang, H. Chen and H. Zhang, Influence of dextrin content and sintering temperature on the properties of coal fly ash-based tubular ceramic membrane for flue gas moisture recovery, *J. Eur. Ceram. Soc.*, 2021, **41**, 5696–5710.

13 M.-q. Yang and J.-y. Yang, Vanadium extraction from steel slag: Generation, recycling and management, *Environ. Pollut.*, 2024, **343**, 123126.

14 M. Rafieizonooz, J. Mirza, M. R. Salim, M. W. Hussin and E. Khankhaje, Investigation of coal bottom ash and fly ash in concrete as replacement for sand and cement, *Constr. Build. Mater.*, 2016, **116**, 15–24.

15 K. Tabit, H. Hajjou, M. Waqif and L. Saadi, Effect of CaO/SiO_2 ratio on phase transformation and properties of anorthite-based ceramics from coal fly ash and steel slag, *Ceram. Int.*, 2020, **46**, 7550–7558.

16 X. Guo and J. Yang, Intrinsic properties and micro-crack characteristics of ultra-high toughness fly ash/steel slag based geopolymer, *Constr. Build. Mater.*, 2020, **230**, 116965.

17 H. Motz and J. Geiseler, in *Waste Management Series*, ed. G. R. Woolley, J. J. J. M. Goumans and P. J. Wainwright, Elsevier, 2000, vol. 1, pp. 207–220.

18 L. Zhao, M. Hu, H. Muslim, T. Hou, B. Bian, Z. Yang, W. Yang and L. Zhang, Co-utilization of lake sediment and blue-green algae for porous lightweight aggregate (ceramsite) production, *Chemosphere*, 2022, **287**, 132145.

19 J. Nie, Q. Wang, S. Gao, C. S. Poon, Y. Zhou and J.-s. Li, Novel recycling of incinerated sewage sludge ash (ISSA) and waste bentonite as ceramsite for Pb-containing wastewater treatment: Performance and mechanism, *J. Environ. Manage.*, 2021, **288**, 112382.

20 Z. Ji, W. Tang and Y. Pei, Constructed wetland substrates: A review on development, function mechanisms, and application in contaminants removal, *Chemosphere*, 2022, **286**, 131564.

21 H. Wang, J. Xu, Y. Liu and L. Sheng, Preparation of ceramsite from municipal sludge and its application in water treatment: A review, *J. Environ. Manage.*, 2021, **287**, 112374.

22 G. Cheng, Q. Li, Z. Su, S. Sheng and J. Fu, Preparation, optimization, and application of sustainable ceramsite substrate from coal fly ash/waterworks sludge/oyster shell for phosphorus immobilization in constructed wetlands, *J. Cleaner Prod.*, 2018, **175**, 572–581.

23 Q. Yu, C. Li, Z. Wang and A. Deng, Study on Preparation and Properties of Unburned Ceramsite With Steel Slag, *IOP Conf. Ser.:Mater. Sci. Eng.*, 2019, **677**, 022067.

24 Y. Sun, J.-s. Li, Z. Chen, Q. Xue, Q. Sun, Y. Zhou, X. Chen, L. Liu and C. S. Poon, Production of lightweight aggregate ceramsite from red mud and municipal solid waste incineration bottom ash: Mechanism and optimization, *Constr. Build. Mater.*, 2021, **287**, 122993.

25 V. O. de Almeida, T. C. Brandao Pereira, L. d. S. Teodoro, M. Escobar, C. J. Ordovas, K. B. dos Santos, J. Weiler, M. R. Bogo and I. A. Homrich Schneider, On the effects of iron ore tailings micro/nanoparticles in embryonic and larval zebrafish (Danio rerio), *Sci. Total Environ.*, 2021, **759**, 143456.

26 L. Wang, Y. Wang, W. Sun and C. Wang, Preparation of lightweight and high-strength ceramsite from highly doped coal fly ash, *Trans. Nonferrous Met. Soc. China*, 2023, **33**, 3885–3898.

27 S. Shang, H. H. Fan, Y. X. Li, L. Li and Z. Li, Preparation of Lightweight Ceramsite from Solid Waste Using SiC as a Foaming Agent, *Materials*, 2022, **15**, 325.

28 C. Peng, G. F. Dai, Y. H. Wang, J. H. Yang and C. X. Wang, Preparation of high-strength ceramsite from coal gangue and printing and dyeing sludge: Design strategy and modelling mechanism, *Ceram. Int.*, 2024, **50**, 19963–19970.

29 Z. J. Song, X. W. Zhang, Y. J. Tan, Q. Zeng and Y. L. Hua, An all-in-one strategy for municipal solid waste incineration fly ash full resource utilization by heat treatment with added kaolin, *Trans. Nonferrous Met. Soc. China*, 2023, **329**, 117074.

30 Y. Zhu, Y. Y. Shao and C. Tian, Preparation of municipal solid waste incineration fly ash/granite sawing mud ceramsite and the morphological transformation and migration properties of chlorine, *Waste Manage.*, 2024, **173**, 1–9.

31 K. J. Tang, H. N. An, C. B. Liu and Y. D. Li, Safety and environmental protection application of high performance solid waste unburned ceramsite and its lightweight high strength concrete, *Sustainable Chem. Pharm.*, 2024, **40**, 101611.

32 J. H. Wang, S. Y. Wang and H. Z. M. Wang, Influence of Ceramsite with Assembly Unit of Sludge and Excavated Soil on the Properties of Cement Concrete, *Materials*, 2022, **15**, 3164.

33 F. Xu, W. Liu, S. Bu, L. Zhang and J. M. Fang, Manufacturing non-sintered ceramsite from incinerated municipal solid waste ash (IMSWA): Production and performance, *Process Saf. Environ. Prot.*, 2022, **163**, 116–130.

34 P. Liu, A. Luo and L. Liu, Study on the preparation and performances analysis of lightweight high strength ceramsite aerated concrete, *J. Mater. Res. Technol.*, 2023, **25**, 6672–6683.

35 L. Q. Tong, J. Q. Ji and J. X. Yang, Sludge-based ceramsite for environmental remediation and architecture ingredients, *J. Cleaner Prod.*, 2024, **448**, 141556.

36 H. M. Hamada, J. Y. Shi and F. Abed, Recycling solid waste to produce eco-friendly ultra-high performance concrete: A review of durability, microstructure and environment characteristics, *Constr. Build. Mater.*, 2023, **876**, 162804.

37 C. W. Wang, Y. X. Wang, W. Sun and L. S. Wang, Thermodynamic assessment of iron and the expansion behavior of porous ceramsite in pure mineral systems relating to solid waste components, *Ceram. Int.*, 2022, **48**, 32867–32876.